JOURNAL OF COMPUTATIONAL PHYSICS 78, 114–137 (1988)

An Implicit Simulation of Drift-Wave Turbulence in a Sheared Magnetic Field

BRUCE D. SCOTT

Institute for Fusion Studies, University of Texas, Austin, Texas 78712

Received October 31, 1986; revised September 21, 1987

An implicit scheme for the simulation of electrostatic fluid turbulence in a magnetic field with spatially varying shear is presented. Large coupling terms representing shear-induced dissipation are evaluated implicitly to avoid severe timestep restrictions. Step order in the scheme is made very important by the added presence of turbulent $\mathbf{E} \times \mathbf{B}$ convection and viscous dissipation. It is shown that the need to temporally resolve resistive dissipation is only important in the regions to which the fluctuations are localised: near the dissipationless resonance layer and at small to moderate wavenumbers. Intermittent phenomena at moderate wavenumbers are shown to play an important role in the essential physics of the turbulence. This causes the need for high spatial resolution, as viscous dissipation must be kept away from the important scales. Convergence tests and linear growth rate checks are performed on the scheme. © 1988 Academic Press, Inc.

I. INTRODUCTION

Collisional drift-waves have at times been thought to contribute to anomalous transport in fusion devices, particularly particle transport in tokamaks [1]. The essential mechanism is for convective $\mathbf{E} \times \mathbf{B}$ fluctuations driven by the density gradient to combine with density fluctuations in such a way to give rise to a net particle flux down the density gradient [2]. This flux must be several orders of magnitude larger than that predicted strictly from collisional transport if it is to explain the observed transport. The free energy source is the density gradient while magnetic shear damping of the associated outward propagating sound waves acts as the sink [3]. An additional sink is provided by the resistive dissipation of parallel currents. Higher order effects such as toroidicity [4] or coupling to trapped electrons [5] are necessary for the waves to be unstable, but these can be modelled by an ad hoc driving term in the equations. For the purpose of studying the essential physics of the turbulence we consider the model of a sheared slab with a density gradient.

Previous numerical treatments of drift-wave turbulence have tended to make use of the adiabatic assumption, in which electrostatic and internal energy in the fluctuations are equipartitioned by diffusive processes on a time scale fast compared to that of the waves, yielding a simplifying relation between the density response and

0021-9991/88 $3.00
Copyright © 1988 by Academic Press, Inc.
All rights of reproduction in any form reserved.

the fluctuating electrostatic potential: $n/n_0 = \exp(e\tilde{\phi}/T)$, or for small fluctuations, $\tilde{n}/n_0 = e\tilde{\phi}/T$. This is the relation used in the absence of magnetic shear to get the Hasegawa–Mima equation [6]. It is convenient because the problem is now reduced to one equation, many treatments of which are tractable analytically. To provide for instability, and a cross-field particle flux, a small phase shift, $\delta_{\mathbf{k}}$, is introduced for each wave [7], so that in wavenumber space one has

$$\frac{\tilde{n}_{\mathbf{k}}}{n_0} = \frac{e\tilde{\phi}_{\mathbf{k}}}{T}(1 - i\delta_{\mathbf{k}}), \tag{1}$$

henceforth referred to as the "i-delta" treatment. This relation has been used even when magnetic shear is included and sound-wave resonant damping gives the treatment a second equation [8]. The necessary condition for the adiabatic relation is $(\rho_e^2 \nu_e/\rho_s^2, k_{||}^2 D_{||})) \gg \omega$, where ρ_e is the electron gyroradius, ρ_s is the ion gyroradius defined using the electron temperature, $k_{||}$ is the component of the wavenumber parallel to the equilibrium magnetic field, and $D_{||} = T_e/m_e \nu_e$ is the parallel electron diffusion coefficient. Since for all but the smallest tokamaks the perpendicular diffusion rate is slow compared to the diamagnetic frequency, $\omega_* \approx \omega$, the condition becomes $k_{||}^2 V_e^2 \gg \omega \nu_e$, where V_e is the electron thermal velocity.

The problem with the i-delta treatment now becomes immediately obvious, because in a real system with shear there is a place where the dominant mode is resonant, where $k_{||}$ vanishes. Assuming that $k_{||}$ is spatially linear near this resonant surface this yields an electron conduction channel, of width $\Delta_D \equiv (\omega_* \nu_e)^{1/2}/k'_{||} V_e$, in which the fluctuations are hydrodynamic, i.e., the flow fluctuations are decoupled from and not driven by those in the density, although the former can still drive the latter. In this region the linear coupling effects, all of which scale with the parallel gradient, are small, leaving nonlinear turbulent convection to dominate the plasma response to the fluctuating potential. Outside the electron conduction channel the fluctuations are adiabatic: any small phase shift would lead to large parallel currents (see Ohm's law in the next section). Thus, one is likely to see appreciable particle flux only in the hydrodynamic regions, even if for a single helicity the electron conduction channel is narrow. (Purely adiabatic fluctuations yield no particle flux.) Clearly, a simple phase relation as in Eq. (1) with constant $\delta_{\mathbf{k}}$'s will fail to represent the correct physics if both regions are present. The hydrodynamic region will be the most important in low-temperature regions such as the tokamak edge, as in such regions Δ_D/ρ_s can be large.

What must be done numerically is not only to have separate time-dependent equations for the density and potential, but also to be able to treat spatially varying coupling terms in both equations. Since large shear regions are present, this gives rise to numerical stability problems. Recent treatments with separate density and potential evolution avoided this by keeping a constant parallel wavenumber, i.e., parallel dissipation was included, but magnetic shear was not [9, 10]. In that case $k_{||}$ is approximated by a constant. The physics problem, of course, is that the fluctuations are no longer shear-localised. In the full problem, the shear terms take

their maximum values at the edge of a sheared slab, where $k_{||} = k'_{||} x_{\max}$. These terms become very large indeed if many modes are kept. The problem is not so bad if the adiabatic relation is used, for in that case the remaining coupling terms involving ion sound waves are much weaker [8]. Presented here is a numerical method to evaluate such terms implicitly, separately (split) from other parts of the algorithm. The method is useful in any case where large, cancelling terms appear linearly to couple two or more equations together. In the next section the model for 2D drift-wave turbulence is presented. Following this are sections describing the numerical algorithm, important questions of resolution not always addressed, identification of coherent structures, and complete testing of the algorithm.

II. The Model

The basic model for nonlinear drift-wave turbulence in this paper is a 2D sheared slab whose coordinate system of unit vectors $(\hat{\mathbf{x}}, \hat{\mathbf{y}}, \hat{\mathbf{z}})$ is defined respectively by the directions of the density gradient, the fundamental wavevector, $\mathbf{k}_0$, and the magnetic field at the resonant surface, where $k_{||} = k'_{||} x = 0$. The two-fluid Braginskii model [11] is used with the assumptions of electrostatic fluctuations ($\tilde{\mathbf{B}} = 0$), a thin resonance layer ($k_0 \Delta_D \ll 1$), and cold ions ($T_i \ll T_e \equiv T$). The scheme of derivation is the same as that used for nonlinear tearing modes and is explained in detail elsewhere [12]. One then has Ohm's law and equations for charge conservation, electron continuity, and parallel ion momentum:

$$\eta \tilde{J}_{||} = \frac{T}{n_0 e} \nabla_{||} \tilde{n} - \nabla_{||} \tilde{\phi},$$

$$\frac{d}{dt} \nabla_{\perp}^2 \tilde{\phi} = 4\pi \frac{v_A^2}{c^2} \nabla_{||} \tilde{J}_{||},$$

$$\frac{d\tilde{n}}{dt} = \frac{1}{e} \nabla_{||} \tilde{J}_{||} - n_0 \nabla_{||} \tilde{u}_{||},$$

$$\frac{d\tilde{u}_{||}}{dt} = -\frac{c_s^2}{n_0} \nabla_{||} \tilde{n} + \mu_{||} \nabla_{||}^2 \tilde{u}_{||},$$

with the last included to provide for the linear damping mechanism of coupling to outward-propagating ion sound waves. It is important to include the $\mu_{||}$ term as this models ion Landau damping of the outgoing waves, which is a major source of dissipation. In numerical terms it is necessary to shear-localise the fluctuations so they do not appreciably interact with the boundary. Standard notation is used throughout, with the convective derivative $d/dt \equiv \partial/\partial t + (c/B)\hat{\mathbf{z}} \cdot (\nabla \tilde{\phi} \times \nabla)$ and the parallel gradient $\nabla_{||} \equiv (x/L_s)(\partial/\partial y)$, where L_s is the shear length. The tilde refers to the fluctuating variables: the background profiles are held fixed so as to focus on the nonlinear physics. If x, y, and t are respectively scaled by $\rho_s \equiv (M_i/m_e)^{1/2} \rho_e$,

k_0^{-1}, and ω_*^{-1}, with $\tilde{\phi}$, $\tilde{n}$, and $\tilde{u}_{||}$ scaled by $(T/e)(\rho_s/L_n)$, $n_0(\rho_s/L_n)$, and $c_s(\rho_s/L_n)$; we have the dimensionless system of equations used in this paper:

$$\frac{\partial}{\partial t}\nabla_\perp^2\phi = -\mathbf{v}\cdot\nabla(\nabla_\perp^2\phi) + C^{-1}\nabla_{||}^2(n-\phi) + D(\nabla_\perp^2\phi), \tag{2}$$

$$\frac{\partial n}{\partial t} = -\mathbf{v}\cdot\nabla n - \frac{\partial\phi}{\partial y} + C^{-1}\nabla_{||}^2(n-\phi) - \frac{L_n}{L_s}\nabla_{||}u + D(n), \tag{3}$$

$$\frac{\partial u}{\partial t} = -\mathbf{v}\cdot\nabla u - \frac{L_n}{L_s}\nabla_{||}n + \mu\nabla_{||}^2 u + D(u), \tag{4}$$

where we have dropped the tildes. Here, the second term in Eq. (3) arises from the background density gradient, $\mathbf{v}\cdot\nabla \equiv \hat{\mathbf{z}}\cdot(\nabla\phi\times\nabla)$, $\nabla_\perp^2 \equiv (\partial/\partial x)^2 + (K\partial/\partial y)^2$, $\nabla_{||} \equiv x(\partial/\partial y)$, and D is a perpendicular operator used solely for numerical purposes to facilitate truncation of the spectrum in **k**-space. In order to study most clearly the character of conservative transfer in the 2D turbulence, we have not included artificial driving. This would enter the density gradient drive term in the xk_y-space representation of Eq. (3) in the form of a multiplier $(1+iy_l)$, for each lth mode. This driving is used in linear growth tests since these tend to fail for damped modes, which have convergence difficulties associated with the outgoing waves. Equations (2)–(4) are evolved within a region of width $2x_L$ about the resonant surface and periodic in y.

The parameters are the ratios $C \equiv (\Delta_D/\rho_s)^2 = (v_e/\omega_*)(m_e/M_i)(L_s/L_n)^2$ and L_n/L_s, with the parallel diffusion coefficient $\mu \equiv \mu_{||}K^2/L_s^2\omega_*$. An additional parameter is the minimum wavenumber scale $K \equiv k_0\rho_s$, which appears in the $\nabla_\perp^2$ operator. The most important of these is C, which determines the electron channel width. In keeping with tokamak ordering L_n/L_s is taken to be small, and then μ is chosen to set the sound wave damping point outside the sound wave resonance point, L_s/L_n, but within the outside limit of computation, where the fields are assumed to vanish. Also, K is taken to be small, but not infinitesimal, as the essential structure size is expected to be of order ρ_s in both the x and y directions. The diffusion coefficient in D is assumed to be sufficiently small that D has no effect at either the largest scales or those at ρ_s sizes.

III. Numerical Algorithm

Upon examination of Eqs. (2)–(4) it is clear that the most damaging contributions to numerical instability are the $\nabla_{||}^2$ terms, proportional in xk_y-space to l^2x^2 for the lth mode, that is, parallel diffusion by electrons must be resolved by the numerical scheme. To see this we consider the simplified system

$$\frac{\partial}{\partial t}\nabla_\perp^2\phi = C^{-1}\nabla_{||}^2(n-\phi), \tag{5}$$

$$\frac{\partial n}{\partial t} = C^{-1}\nabla_{||}^2(n-\phi), \tag{6}$$

to isolate the effects of these terms. This is the subsystem representing electron adiabatisation. The linear numerical stability of Eqs. (5), (6) is determined for one mode in xk_y-space. Time-differencing is done by replacing $\partial f/\partial t$ with $(f-f^0)/\tau$, where τ is the timestep and the superscript "0" denotes evaluation at the immediately previous step. We replace $\nabla_{||}^2$ with $-l^2x^2$, where l is the mode number, and $\nabla_\perp^2$ with $-k^2 \equiv -2g/(\Delta x)^2 - l^2K^2$, where Δx is the step size in the x-direction. The multiplier g may take on values from $\frac{1}{2}\pi^2(\Delta x)^2/x_L^2$ to 2, i.e., we evaluate the finite-differencing in terms of the possible k_x values [13]. A purely explicit scheme with which to evolve Eqs. (5), (6) may be expressed as

$$\begin{pmatrix}\phi\\ n\end{pmatrix} = \begin{pmatrix}1-\tau L^2k^{-2} & \tau L^2k^{-2}\\ \tau L^2 & 1-\tau L^2\end{pmatrix}\begin{pmatrix}\phi^0\\ n^0\end{pmatrix},$$

where $L^2 \equiv C^{-1}l^2x^2$. The eigenvalues of the amplification matrix (the 2×2 matrix) must all lie within the unit circle in the complex plane for the scheme to be stable. Evaluation of these eigenvalues shows them to take the values unity or $\gamma = 1-\tau L^2(1+k^{-2})$. Regardless of the value of k, this scheme will be unstable if the timestep violates the condition

$$\tau < 2L^{-2} = 2Cl^{-2}x^{-2}. \tag{7}$$

This is clearly a catastrophic constraint, since $C^{-1}x_L^2$ is at least 100 (see the next section) and several tens of modes must be kept in order to resolve the turbulent structure dynamics.

In contrast to this, the main contributor to the timestep limit in 2D electromagnetic codes is the parallel Alfvén wave, whose equation sets the double time derivative against the $\nabla_{||}^2$ operator:

$$\frac{\partial^2}{\partial t^2} \leftrightarrow \nabla_{||}^2,$$

or, upon finite time-differencing,

$$\frac{1}{\tau^2} \leftrightarrow l^2x^2.$$

However, in the case of drift waves there is only one time derivative balancing the parallel diffusion terms: here we have

$$\frac{1}{\tau} \leftrightarrow l^2x^2,$$

an extra factor of lx worse, leading to the timestep constraint given in Eq. (7). In the i-delta treatment the problem does not arise: there are no $\nabla_{||}^2$ terms because they cancel in the derivation of the Hasegawa–Mima equation (subtracting Eq. (2) from Eq. (3)) [6]. This leaves only the single $\nabla_{||}$ operator in the sound-wave coupling terms, and these are multiplied by a small coefficient. In the constant-$k_{||}$ case there is neither x- nor k_y-dependence to the coupling terms, so the restriction of Eq. (7) is largely eliminated. For shear-flow problems with magnetic shear it is a simple matter to evaluate the offending term at the current time step as it does not couple to another equation. One need only invert the operator

$$\nabla_\perp^2 - \tau l^2 x^2,$$

as a tridiagonal matrix. The tridiagonal is necessary because both the gradient and the spatial dependence enter squared, so that Fourier transforming does not help.

The problem with Eqs. (2)–(4) is that the $\nabla_{||}^2$ terms (shear terms) couple two equations. To evaluate them in an implicit manner requires a folded manipulation in which n is eliminated in favor of ϕ, the resulting equation for ϕ is solved, and then the scheme is "unfolded" by solving for the new n in terms of the new ϕ. These are used to get the new $\nabla_\perp^2 \phi$ without operating with with $\nabla_\perp^2$. In the complete scheme the timestep is split, as the nonlinear convection and D operators are each handled separately from the part dealing with the shear terms. Thus, the scheme is necessarily only first-order accurate in the timestep, as terms of second order in τ are discarded.

We illustrate the new method once again using Eqs. (5), (6), without the sound waves, to show that the $\nabla_{||}^2$ terms are stabilised. From the implicit evaluation of the shear terms,

$$\nabla_\perp^2 \phi = \nabla_\perp^2 \phi^0 - \tau L^2 (n - \phi),$$
$$n = n^0 - \tau L^2 (n - \phi)$$

(where the superscript "0" refers to the previous time step) we first solve for n to obtain

$$n = \frac{n^0 + \tau L^2 \phi}{1 + \tau L^2}.$$

This is then used to eliminate n in the ϕ-equation:

$$\left(\frac{\tau L^2}{1 + \tau L^2} - \nabla_\perp^2 \right) \phi = \frac{\tau L^2}{1 + \tau L^2} n^0 - \nabla_\perp^2 \phi^0.$$

Evaluating the finite-differencing as before, this scheme may be expressed in matrix form as

$$\begin{pmatrix} n \\ \phi \end{pmatrix} = \begin{pmatrix} \dfrac{1}{1+\tau L^2} & \dfrac{\tau L^2}{1+\tau L^2} \\ 0 & 1 \end{pmatrix} \begin{pmatrix} 1 & 0 \\ \alpha^{-1}\tau L^2 & \alpha^{-1}k^2(1+\tau L^2) \end{pmatrix} \begin{pmatrix} n^0 \\ \phi^0 \end{pmatrix},$$

where $\alpha \equiv \tau L^2 + k^2(1+\tau L^2)$. The amplification matrix is the product of the two matrices in this equation, and its eigenvalue, γ, is determined by

$$(\alpha\gamma)^2 - [\alpha + k^2](\alpha\gamma) + \alpha k^2 = 0.$$

Again along with unity, the variable eigenvalue of the new amplification matrix is

$$\gamma = \frac{k^2}{\tau L^2 + k^2(1+\tau L^2)},$$

which lies within the unit interval for all values of τ, regardless of k or L. Note that the value of unity is no longer trivial, as it indicates marginal stability for all parameter values. However, we do know that large timesteps are not numerically pathological, i.e., this part of the overall system is never unstable. The overall numerical stability will now be determined by the cascade processes in the nonlinear convective terms, as it is impractical to evaluate these implicitly.

Two notes must be pointed out. The first is that if the timestep is too large, the density fluctuations will exhibit too much adiabaticity. If τ is not very much less than unity the factor $\tau C^{-1} I^2 x^2$ can be appreciable inside the layer. Numerically, this factor controls adiabaticity, not C by itself. As τ increases the fluctuations become more and more adiabatic until the results are no longer correct, even if there are no obvious problems with the scheme. Thus, one must still be sure to accurately resolve the parallel diffusion process within the hydrodynamic layer and where the fluctuations are appreciable even though this may not be necessary in other regions. This consideration limits the timestep to values on the order of 10^{-3} (see tests below). The other note is that the order of operations is very important. The way in which the eliminations are made guarantees that the factor τL^2 never appears by itself, but always in the form of $\tau L^2/(1+\tau L^2)$. Thus, if τL^2 is large the acting operator is of order unity. Cancellations between large terms are automatic rather than forced, and n will asymptotically relax to ϕ rather than try to track it. If standard inversion of the block tridiagonal of 2×2 elements is attempted this benefit will be lost.

If the magnetic shear were very strong $[L_n/L_s \sim O(1)]$ it would be necessary to do this with the sound wave as well. The procedure works the same way as for the simplified system analysed above. The first elimination is of u in favor of n, after which the procedure continues in the preceding illustration. In actual practice, however, this is not necessary in cases of tokamak ordering $[(1, C^{-1/2}) > L_n/L_s]$, and in this work the sound wave is left explicit and is simply added into n^0. Note that the parallel viscosity, a homogeneous term, is still evaluated implicitly.

The difference equations which represent Eqs. (2)–(4) are

$$\nabla_\perp^2 \phi = \nabla_\perp^2 \phi^0 - (\mathbf{v}\cdot\nabla\nabla_\perp^2\phi)^p - \tau C^{-1} l^2 x^2 (n-\phi) + \tau D(\nabla_\perp^2 \phi),$$
$$n = n^0 - (\mathbf{v}\cdot\nabla n)^p - \tau C^{-1} l^2 x^2 (n-\phi) - i\tau l\phi^0 - i\tau (L_n/L_s)\, lxu^0 + \tau D(n),$$
$$u = u^0 - (\mathbf{v}\cdot\nabla u)^p - i\tau (L_n/L_s)\, lxn^0 - \tau\mu l^2 x^2 u + \tau D(u),$$

where the superscript "p" refers to the predictor-corrector used on the nonlinear convection terms. Although the sound wave terms are labelled with the "0" they are evaluated after the convection operators.

The first stage is the convection operation. This is a standard predictor-corrector [13] with a predictor step of 0.5τ,

$$n^* = n^0 - 0.5\tau(\mathbf{v}\cdot\nabla n)^0, \tag{8a}$$
$$n^p = n^0 - \tau(\mathbf{v}\cdot\nabla n)^*, \tag{8b}$$

for each quantity, $\nabla_\perp^2\phi^p$, n^p, u^p, with ϕ^* being obtained from the tridiagonal inversion of $\nabla_\perp^2$ on $\nabla_\perp^2\phi^*$. Next, the shear and drive terms are evaluated:

$$n^s = n^p - i\tau l\phi^0 - i\tau(L_n/L_s)\, lxu^p, \tag{8c}$$
$$\nabla_\perp^2\phi^s = \frac{\tau C^{-1} l^2 x^2 n^s}{1+\tau C^{-1} l^2 x^2} - \nabla_\perp^2 \phi^p, \tag{8d}$$
$$u^s = (1+\tau\mu l^2 x^2)^{-1}\,[u^p - i\tau(L_n/L_s)\, lxn^p]. \tag{8e}$$

In Eq. (8c), ϕ appears as ϕ^0; this is in order to save an extra tridiagonal operation after the evaluation of Eq. (8b). It does not affect the performance of the scheme, as this term is much "slower" than the shear terms. The viscous operator is inverted here immediately after the explicit evaluations have caused the most trouble at high l:

$$n^d = (1-\tau D)^{-1}\, n^s, \tag{8f}$$

for each quantity, $\nabla_\perp^2\phi^d$, n^d, u^d. Note that u^d is u at the current timestep as the scheme has finished for that quantity. This is followed by the implicit shear inversion and the unfolding illustrated on the simplified system above:

$$\phi = \left(\frac{\tau C^{-1} l^2 x^2}{1+\tau C^{-1} l^2 x^2} - \nabla_\perp^2\right)^{-1} \nabla_\perp^2 \phi^d, \tag{8g}$$
$$\nabla_\perp^2\phi = \frac{\tau C^{-1} l^2 x^2}{1+\tau C^{-1} l^2 x^2}\,\phi - \nabla_\perp^2\phi^d, \tag{8h}$$
$$n = \frac{n^d + \tau C^{-1} l^2 x^2 \phi}{1+\tau C^{-1} l^2 x^2}. \tag{8i}$$

The step order is very important, for because the shear inversion scheme is marginally stable, the sound waves are explicit, and the predictor-corrector is actually mildly unstable the inversion of D must occur exactly where it has been put. Anywhere else it is unable to stop the growth of small scale disturbances unless it is made too large. Because of this, direct operation by $\nabla_\perp^2$ must be avoided. Thus, $\nabla_\perp^2 \phi$ is obtained instead from Eq. (8h). The density is then allowed to follow ϕ without interference from other operators. Such interference would be the case if D were inverted at the very last.

In Eqs. (8a), (8b) the $\mathbf{v}\cdot\nabla$ terms are evaluated in xy-space, i.e., the code is pseudospectral in y. The problem of aliasing [14] in the convolutions is avoided by restricting the total number of k_y-modes to $\frac{2}{3}N_y$, where N_y is the number of grid points in the y-direction. The number of modes is actually not $\frac{2}{3}N_y$ but half that as a result of the reality condition in which $\phi_{-l}(x)$ is replaced by the complex conjugate of $\phi_l(x)$. Thus, the grid will be $N_x \times N_y$ in real space, or $N_x \times \frac{1}{3}N_y$ in xk_y-space.

Again, because of the x^2 in the shear terms the scheme is finite-differenced in the x-direction, as nothing would be gained by transforming to $k_x k_y$-space, changing the x^2 term into a $\partial^2/\partial k_x^2$ operator. On the other hand, it may be desirable to do the D inversions in $k_x k_y$-space (assuming no spatial dependence in D), especially if the finite-difference approximation to D involves more than three diagonals in the matrix, as is the case if a hyperviscosity is used. (Note that the localisation confers the benefits of zero-packing for the FFT operations.) In this paper we use the hyperviscosity, so that

$$D = -\mu_\perp \nabla_\perp^4, \tag{9}$$

keeping the dissipation range to the highest k's (see below and the next section). On the other hand, it is necessary to invert the $\nabla_\perp^2$ operator of Eqs. (8b), (8g) in xk_y-space as a tridiagonal matrix to avoid difficulty with boundary conditions, which are built-in with the matrix but difficult to handle in $k_x k_y$-space. This creates additional numerical dissipation which must be lived with because the difficulty of localising the $lK \sim 1$ modes prohibits the latter approach.

The problem with $x \leftrightarrow k_x$ transforms is that a constant grid spacing must be used. In some cases this has the undesirable effect of forcing high resolution everywhere if it is needed anywhere. One must simply decide whether this disadvantage is outweighed by the beneficial effects of the hyperviscosity. In the drift-wave case it is, because of the need for a nearly inviscid intermediate range in the spectrum. In any case, the high resolution (see next section) is necessary in the high-shear regions to resolve the accompanying outgoing waves. For the grid size used here the FFTs used in the inversion of D have been seen to take roughly the same computational effort as the tridiagonal inversions.

The code was initially run with a diffusion operator in xk_y-space of

$$D = \mu_\perp l^4 \nabla_\perp^2, \tag{10}$$

so that xk_y-space needed only be left when doing the pseudospectral convolutions

in the nonlinear $\mathbf{v} \cdot \nabla$ operator. This gave a sort of average of k^4, roughly sixth order in k_y and second order in k_x. However, in shear-flow tests this did not adequately cut off the k_x-spectrum, so the more isotropic hyperviscosity is now used. The estimation of viscous Reynolds numbers (nonlinear convection/viscous damping) for such an operator is also made easier (see Ref. [15]). Indeed, the D operator is necessary for k_x, not k_y. Shear dissipation is more than adequate in cutting off the k_y-spectrum at small scales. The fact that shear dissipation is in balance with driving everywhere in the spectrum indicates that the Reynolds number with respect to magnetic shear is of order unity. However, there is no k_x-dissipation in the $\nabla_{||}$ operator, so D is needed to do the truncation in k_x. Also, bad behaviour at high-k_x will affect high-k_y as well due to the tendency of small-scale turbulence to isotropise. One might like an even steeper cutoff resulting from an even higher order operator, but this can lead to irregularities in the spectrum near the $D_l \sim 1$ boundary (at $lK \sim \mu_\perp^{-1/\alpha}$, using $D = \mu_\perp (\nabla_\perp^2)^{\alpha/2}$). On the other hand, the more physical Newtonian viscosity,

$$D = \mu_\perp \nabla_\perp^2,$$

does not work because the dissipation range in **k**-space is too broad to achieve high viscous Reynolds numbers at the intermediate scales. That is, it is undesirable to have the artificial D operator play much of a role in the physics of the turbulent structures, which in a real plasma are practically inviscid. The hyperviscosity in Eq. (9) was chosen as an adequate compromise, and has been used for similar reasons in the study of coherent structures in decaying Navier–Stokes turbulence [16].

It is possible, but not necessary, to have differing perpendicular diffusion operators in each of the equations. This has been tried in using a smaller "particle diffusion coefficient" (the D in Eq. (3)) than the "perpendicular viscosity," in particular, to set the former to zero. It was found not to be sufficient only to have the artificial diffusion in one or some of the equations, e.g., the neglect of D in Eq. (3) causes problems for the density spectrum even though that for the potential is well behaved at high l. Additionally, this also causes spurious driving, because extra viscosity in Eq. (2) gives rise to more lag between n and ϕ, i.e., more extraction of energy from the density gradient. Since D is artificial, it is simplest to use the same operator in all the equations as this saves space in the computer. One need only be sure that the diffusion is not allowed to play any role in the physics of the turbulence.

The scheme outlined in this section was evolved to handle the problems of 2D drift-wave turbulence, but the general method should be useful in any case that separate equations are coupled by linear terms which would contribute decisively to numerical instability were they to be evaluated at the previous timestep. If the coupling terms are nonlinear, as in electromagnetic codes where $\nabla_{||}$ is another convolution operator, such a simple solution as this would not work. A more complicated scheme such as the semi-implicit method used in 3D dynamo simulations [17] would have to be resorted to.

IV. Resolution Consideration

The question of **k**-space resolution in numerical treatments of drift-wave turbulence is very important but often neglected. In particular, there are three space scales in the problem which must be separated. These are the macroscopic gradient scale or experimental system size, represented here by k_0^{-1} or L_n, the most probable structure size, or the intermediate scale here typically on the order of a ρ_s, and the smallest scales at which the numerical or artificial dissipation is acting to truncate the spectrum. Truncation is necessary because of the finite size of computer core memory, but the cascade process acts to pile energy at the highest k's since there are none higher to which it can be transferred. The operator D serves to remedy this by dissipating the extra energy in lieu of the cascading. However, a real plasma has such a high viscous Reynolds number that any important scales are practically inviscid. This is the reason the ρ_s scales must be kept out of the dissipation range of D. Most previous drift-wave computations have neglected this consideration [8–10], leading to the erroneous conclusion that only the largest scales play important roles in the physics. It is also important to separate the ρ_s scales from the largest to allow any structures which may form to interact on the largest scales.

What is meant here by "viscous Reynolds number" is a measure of the relative sizes of driving or convection and the artificial diffusion term containing D in a given equation. The real Reynolds number of the entire system will involve a complicated combination of perpendicular and parallel dissipation and the various couplings. Since one looks only for some idea of the scales at which the D terms begin to have importance, the viscous Reynolds number is defined in normalised units as $\omega_l/\mu_\perp(lK)^4$ for the hyperviscosity in Eq. (9), where the numerator enters as a result of normalising the D operator with respect to $k_0 v_D$, and l is the mode number. This is in a sense a "linear" Reynolds number because we have defined it to be amplitude-independent. Using the linear frequency $\omega_l = l/[1+(lK)^2]$, one arrives at the definition $[(\mu_\perp l^3 K^4)(1+l^2K^2)]^{-1}$ for the viscous Reynolds number at the lth mode. (Or, $(\mu_\perp l^5 K^6)^{-1}$ for $lK \gg 1$.) This has been found very useful in locating the dissipation range boundary in k_y-space for the purpose of keeping it away from the important scales. The computations presented in Section VI (except for the test of $\mu_\perp$-dependence) were all performed with $\mu_\perp = 10^{-3}$ and $K = 0.1$, setting the viscous Reynolds number to unity at mode 63 (roughly the viscous dissipation range boundary) and 5×10^3 at mode 10 (also the $k_y\rho_s = 1$ point). The grid resolution is 256×256, which limits the k_y-spectrum to 85 modes so as to automatically avoid the aforementioned aliasing arising from the convolution operations in the nonlinear coupling terms. These smallest scales are highly dissipative under the D operator used. At this size the form of D (either of Eqs. (9), (10)) has been seen to have no important effect on the k_y-spectrum up to the viscous dissipation range, which is what is desired. Tests involving the size of D are presented in Section VI.

In the x-direction it is important to resolve the smallest of Δ_D and ρ_s with of order 10 points and still keep reasonable separation between all the x-scales in the problem. This is needed in the adiabatic regions as well to resolve the outgoing

waves present in the system. The wall at x_L, where the fields are assumed to vanish, must be sufficiently far from the resonance layer that the forced vanishing of all the fields does not reflect outwardly propagating wave energy back into the system. The drift waves couple to ion sound waves near $x = L_s/L_n$, the point at which $k_{\|} c_s$ is equal to the diamagnetic drift frequency. The sound waves then carry energy out and begin to dump it near $x_i = \mu^{-1/2}$, the point at which the drift frequency is equal to the parallel dissipation rate of the outgoing waves, $\mu_{\|} k_{\|}^2$. All of these processes must be well contained within the walls. This requires in practice that x_L be at least twice x_i. Tests have shown 256 points to be the minimum to achieve these conditions (see Section VI). Most previous treatments have avoided this demanding requirement by neglecting magnetic shear, so that an isotropic spectral code may be used [9, 10]. The problem, of course, is that the physics of spatially varying shear, present in all real systems, are invisible to such a treatment. Note lastly that the need for high resolution is what creates such a problem for numerical stability in the first place. The shear terms in Eqs. (2)–(4) would not be so difficult if only a few modes were kept.

V. Coherence Diagnostics

Before discussing the results and numerical tests of the code, we digress with a few words on coherent structures in the turbulence. These are by definition any recognisable forms in one or more of the fields that persist for a long time compared to the correlation time of the turbulent fluctuations. In a recent study of decaying Navier–Stokes turbulence, coherent vortices were observed to form in an initially Gaussian-randomised fluctuation field and then persist throughout the computations [16], some of which were carried out for tens of correlation times. It is important to use a system of numerical diagnostics in studying these structures due to the fact that the eye is a notoriously poor judge on whether or not a given distribution is random. One such test that is easily implemented is the *kurtosis*, or flatness, defined for zero-mean fluctuations as the ratio of the fourth moment to the square of the second: $\mathrm{Ku}(\phi) \equiv \langle \phi^4 \rangle / \langle \phi^2 \rangle^2$, where the angle brackets represent an ensemble average [18]. For time coherence information the time average is used; for spatial intermittency, the averaging becomes an integration over all space. Suitably normalised, this has the value three for a perfectly random, Gaussian distribution. This becomes a very useful diagnostic when the phenomenon under study is not in a stationary state, in which case time correlation measurements are very difficult. A given structure can be followed in successive contour plots, and the kurtosis measurement is used to determine its self-coherence.

Unfortunately, the qualification "suitably normalised" is significant when dealing with localised fluctuations. Clearly, localisation introduces a non-random element into their distribution. Consider, for example, a case of perfect localisation, i.e., fluctuations $\phi(x, y)$ which are nonzero only within some window $x < x_W$. As long as the averages in the definition of $\mathrm{Ku}(\phi)$ include the entire region $(-x_W, x_W)$, the

signal will be proportional to the integration boundary because of the normalisation of the integrals. In practice, the kurtosis measurement must be compared with that of a fluctuation distribution known to be random-phase. The initial state (see the next section) may be used for this. What one is left with is a rather approximate indication of self-coherence rather than a precise diagnostic. We shall see, however, that the situation will be reasonably clear. The kurtosis measurements in this work were all done with an integration limit of 10.0 in the x-direction, i.e., well outside the region within which the fluctuations are well confined.

VI. Numerical Tests and Results

Prior to conducting tests on the full nonlinear scheme the shear term part of the algorithm was tested in a series of linear runs. This entails the scheme as outlined in Eqs. (8c)–(8i), that is, leaving out the convection operators. Linear runs are initialised with a spatial Gaussian for ϕ, with $n=\phi$ and $u=(L_n/L_s)\,x\phi$, the latter a natural form suggested by Eq. (4). These are carried out until all the growth rates, defined as $\frac{1}{2}E_i^{-1}\,\partial E_i/\partial t$ for each ith piece as well as the total energy, converge to equal values. (The factor of two is due to the fact that the E_i's are proportional to the amplitude squared.) The total energy is defined as

$$E \equiv \tfrac{1}{2}\langle|\nabla_\perp \phi|^2\rangle + \tfrac{1}{2}\langle n^2\rangle + \tfrac{1}{2}\langle u^2\rangle, \tag{11}$$

where the angle brackets indicate integrations over all space, the form of which are $\langle\phi\rangle \equiv \int_{-x_L}^{x_L} dx \int_{-\pi}^{\pi} (dy/2\pi)\phi$. The energy conservation law is derived by operating on Eq. (11) with $E^{-1}(\partial/\partial t)$ and using the right sides of Eqs. (2)–(4) to evaluate the derivatives:

$$\gamma_{\text{error}} = E^{-1}\left[\frac{\partial E}{\partial t} + \left\langle n\frac{\partial\phi}{\partial y}\right\rangle + C^{-1}\langle|\nabla_{||}(n-\phi)|^2\rangle + \mu\langle|\nabla_{||}u|^2\rangle\right] + O(\mu_\perp), \tag{12}$$

where γ_{error} represents the growth rate of spurious energy. We may drop the D terms since we are interested only in appreciable errors. It is sufficient to ensure that $\gamma_{\text{error}} \lesssim O(\mu_\perp)$. The three averaged terms represent the energy extracted from the density gradient, resistive dissipation in the hydrodynamic region, and Landau damping of outgoing sound waves, respectively. Equation (12) is thus used to measure the energy conserving capability of Eqs. (8a)–(8i).

We mention "growth rates" because in linear cases it is necessary to drive the equations with a multiplier of $(1+i\gamma_d)$ on the density gradient drive term. The initial state can be thought of as a superposition of the actual eigenfunction and an unwanted addition. The runs will only converge if the eigenfunction grows faster than or damps more slowly than the rest of the initial state. Because of the presence of a free energy source (the density gradient) any spurious relation between n and ϕ can cause the unwanted piece to win. Generally, if the eigenmode has an

appreciable growth rate it will win and the run will converge. However, a damped eigenmode will lose. Thus, it must be driven. Comparison with a result from an analysis or a shooting code may be done after the drive is subtracted. The multiplier is in effect an addition of a complex part to the diamagnetic frequency, so it has the correct form, since the mode frequency is close to ω_* in the first place. (Note that driving is unnecessary in the nonlinear regime because the turbulent convection dominates the character of the fluctuations and so long as $C^{1/2}$ is sufficiently less than L_s/L_n this is not very sensitive to the outgoing waves.) Strictly speaking, this will work only if $(\gamma_d, \gamma_L) \ll \omega_*$ and $K \ll 1$ (γ_L is the actual linear growth rate). However, the first requirement is not too severe, as the following comparison shows.

Figure 1 displays the results of a series of linear runs with $L_n/L_s = 0.2$, $K = 0.1$, $\mu = 0.02$, $x_L = 20.0$, $\mu_\perp = 10^{-3}$, and the timestep $\tau = 10^{-3}$. The solid line gives the shooting code determinations of γ_L for 43 values of C [19]. The dots are the results from the runs. A driving of $\gamma_d = 0.4$ was used for all runs except $C = 3.0$ and 5.0 for which $\gamma_d = 0.5$ and $C = 10.0$ for which it was 0.6. The γ_d's were then subtracted from the resulting growth rates to give the values of γ_L indicated by the dots. Over a wide range of C the initial value scheme gives very accurate results which begin to fail only with insufficient resolution ($C < 0.1$) or sound wave damping ($C \gtrsim 3$, as there is enough coupling to sound waves to defeat localisation within x_L).

We may further check the accuracy of the implicit scheme by varying the timestep on the $C = 1.0$ run between 10^{-5} and 10^{-2}. The results of this test appear

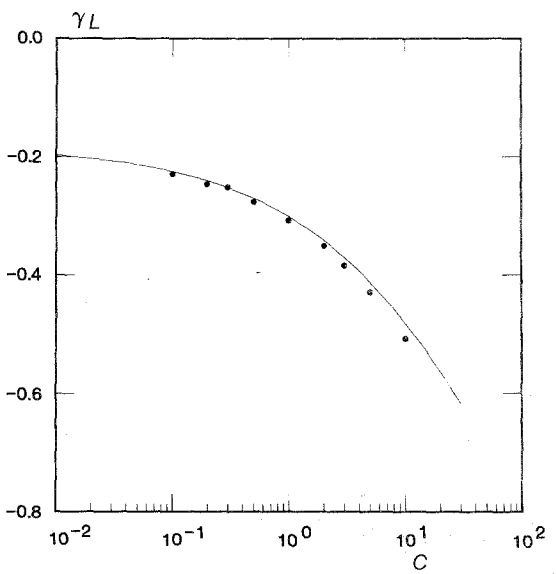

FIG. 1. Comparison of linear growth rates (γ_L) obtained from the implicit scheme (dots) and from a shooting code (line). See text for explanation of extraction of damping rates from the initial-value scheme.

value normally used.

To ensure that the placement of the boundary ($x = x_L$) does not influence the results we vary the value of x_L on the $C = 1.0$ run of Fig. 1 between 10.0 and 50.0. The resulting damping rates are seen in Fig. 3. Precise convergence is seen for $x_L \geqslant 20.0$. These results were identical to four decimal places except for the failure at $x_L = 10.0$. Since the ion resonant damping point is near $x = 7.0$ this is due to lack of sufficient space for mode localisation. Thus, we see the need to keep the boundary at least twice as far from the resonant surface as the ion damping point. The conservation of energy for the $x_L = 50.0$ case was measured using Eq. (12), and γ_{error} was found to be of order few $\times 10^{-4}$. Satisfied by these test we now proceed with tests of the entire algorithm on nonlinear runs.

The computations are initialised with ϕ and n set equal to each other, and u set to $(L_n/L_s)\, x\phi$. The initial field for ϕ is an isotropic, random-phase Gaussian realisation with an amplitude spectrum given by $|\phi|_k \propto k/[1 + (k\rho_s)^4]$, multiplied by a spatial gaussian envelope to reflect localisation to the resonant surface due to magnetic shear, then normalised so that the rms velocity fluctuation is 2.0, i.e., in the nonlinear regime. A picture of this distribution and its spectrum is shown in Fig. 4. It has a measured kurtosis of $\text{Ku}(\phi) = 10$, which is used as a benchmark for these measurements. The fluctuations are not expected to remain adiabatic for long, as the density gradient and nonlinear couplings act to force n and ϕ apart, but this is a reasonable initial state because the most dangerous terms in Eqs. (2)–(4) cancel initially, allowing the fields to find the appropriate time-dependent solution with

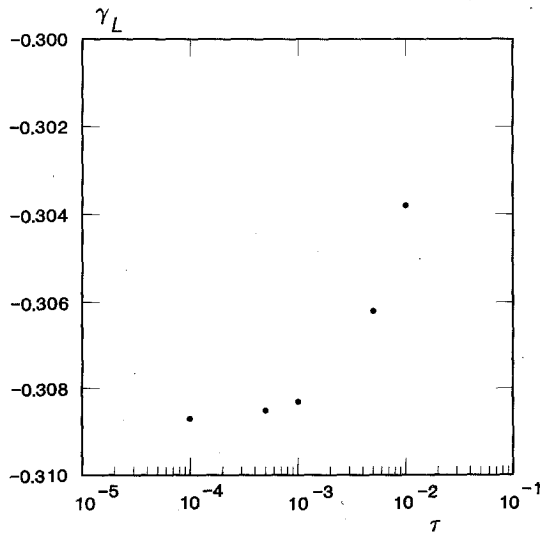

FIG. 2. Convergence check of γ_L against the timestep (τ) in the linear scheme. Note the sharp change for $\tau > 10^{-3}$.

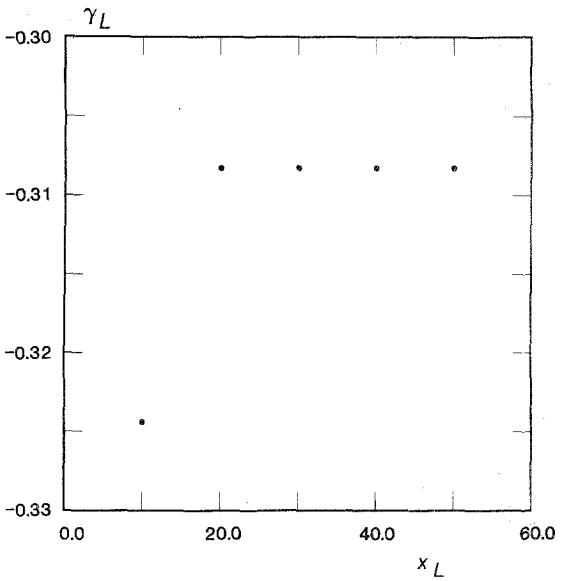

FIG. 3. Convergence check of γ_L against the boundary (x_L) in the linear scheme. Values of x_L between 20.0 and 50.0 gave identical results.

minimal violence. Coherent structures are not assumed at the beginning but may form as the fields evolve. This initial state is then advanced according to the complete algorithm in Eqs. (8a)–(8i).

The typical run consists of a rapid transient phase in which the fluctuations adjust to a state in which the nonadiabatic piece of the density response, h, has risen from zero and become confined within the electron conduction channel, and

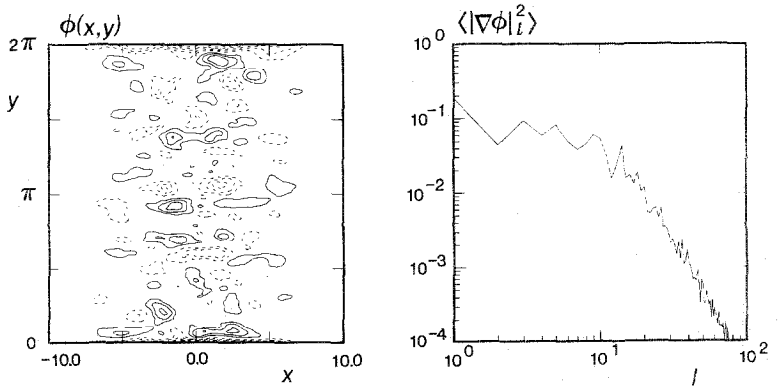

FIG. 4. Contours showing the form of the initial fluctuation distribution $\phi(x, y)$. Solid contours indicate positive values; dotted, negative. The interval is linear. The amplitude energy spectrum is also shown; angle brackets reflect an integration over x. l is the mode number. $\mathrm{Ku}(\phi) = 10$.

then a long decay phase characterised by the dominance of a few large coherent structures in h. The basic features of one such run are depicted in Fig. 5. This was carried out with $C=1.0$, $L_n/L_s=0.2$, $K=0.1$, $\mu=0.02$, $x_L=20.0$, $\mu_\perp=10^{-3}$, and the timestep $\tau=10^{-3}$. The fluctuation contours of ϕ, n, and h are shown at $t=8.0$. The zero contour is suppressed for clarity. The most obvious property is the general localisation to the vicinity of the resonant surface. This is the strongest for h, as electron parallel diffusion strongly damps this quantity outside the electron conduction channel. Localisation in n and ϕ is due to overall magnetic shear damping. The structure in h is also much more complicated than that in either n or ϕ. (Note the linking of the small structures into the large ones.) This is borne out by the kurtosis measurements, which yield $\mathrm{Ku}(h)=29$, while $\mathrm{Ku}(\phi)=10$ and $\mathrm{Ku}(n)=11$ (that of the randomised initial state is 10). More important than the absolute values is the

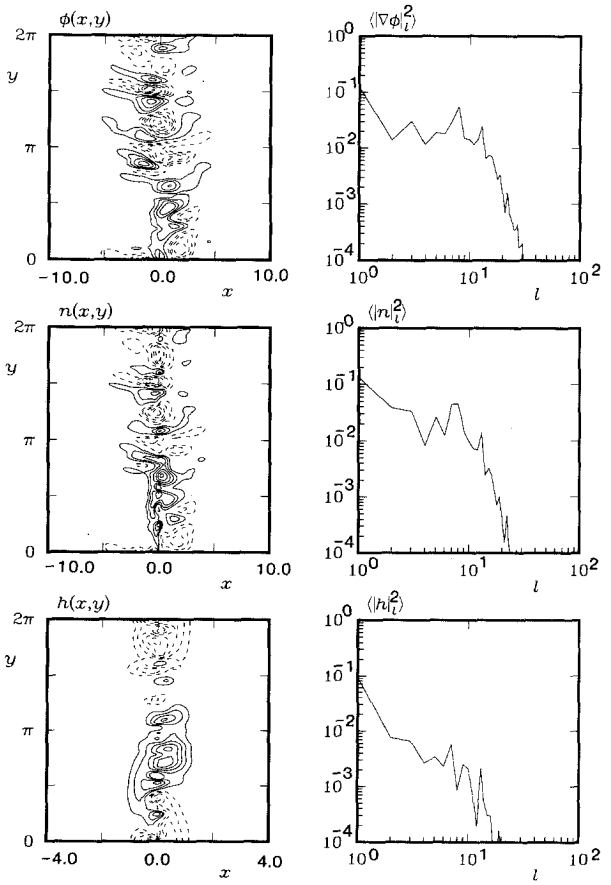

FIG. 5. Contours (as in previous figure) and spectra of a typical run ($C=1$, see text). Note the scale expansion for clarity in the nonadiabatic density (h) contours. l is the mode number. Snapshot at $t=8.0$.

fact that the kurtosis in h is a factor of 3 or so higher than that in either n or ϕ. Besides the obvious self-coherence, this indicates that the character of h is so different from the other fields that a simple phase relation between n and ϕ like that in Eq. (1) cannot suffice. The actual relation is highly spatially dependent, as is clear from the adiabaticity of the fluctuations in the high-shear regions. This demonstrates the need for a way to correctly and completely handle the $\nabla_{\|}^2$ terms in Eqs. (2)–(4), as they will be present in any drift-wave system consisting of both high- and low-shear regions. The energy conservation of just the nonlinear terms was monitored by measuring $\langle \phi^0[\mathbf{v}\cdot\nabla(\nabla_\perp^2\phi)]^*\rangle$, $\langle n^0(\mathbf{v}\cdot\nabla n)^*\rangle$, and $\langle u^0(\mathbf{v}\cdot\nabla u)^*\rangle$ in Eqs. (8a), (8b), where the superscript "0" refers to evaluation at the immediately preceding timestep and "*" to the second evaluation of the convection operators. These were found to fluctuate around zero with an amplitude of order 10^{-7}.

The importance of the intermediate scales is shown by the second half of Fig. 5, in which appear the spectra of ϕ, n, and h. Superimposed upon the mid range background of the density spectrum is a pronounced maximum in the region $k_y\rho_s \gtrsim 1$. The strength of the largest scale reflects the combination of the smaller structures into larger ones. The latter feature is most evident in h, as the coherent structures there are the most dominant. This is where the necessity of high resolution and low dissipation enters, for if either were relaxed these phenomena would not be correctly reproduced. The roles of the intermediate scales would be missed and the conclusion that the largest scales are the only important ones would be reached. However, since the present purpose is the test of a numerical scheme,

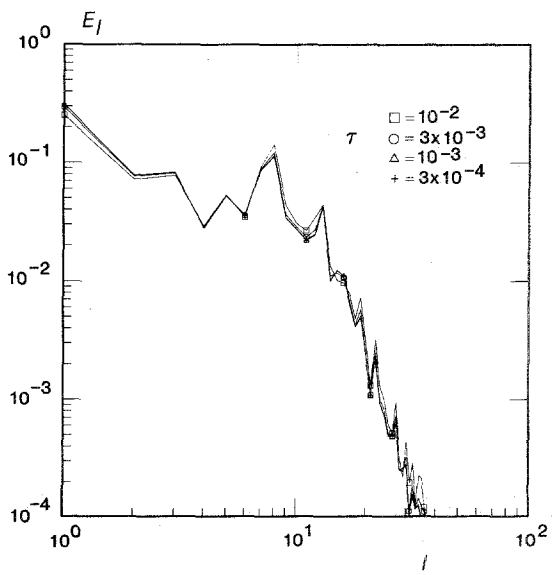

FIG. 6. Effect on the total energy (E) spectrum of varying the timestep. Individual spectra are labelled with the marker shown according to the value of τ used. l is the mode number.

further comment on the physics issues of the turbulence is deferred to later work currently under preparation.

To test the numerics the fields at $t = 6.0$ were pulled from the above run and used in initial conditions for short test runs in which τ, $\mu_\perp$, and x_L were varied. A convergence test on the timestep was first performed. The fluctuations at $t = 6.0$ were started in four runs with τ's of 10^{-2}, 3×10^{-3}, 10^{-3}, and 3×10^{-4}, each carried for two ω_*^{-1}-times. The total energy spectra at the end of these runs are shown in Fig. 6, superposed upon one another. The spectra are labelled with markers corresponding as shown to the above timesteps. They are in good agreement at all scales up to slight departures for $\tau = 10^{-2}$. The time dependence is seen in the evolution curves for the total energy growth rate, which appear in Fig. 7, labelled as in the previous figure. As the timestep becomes larger the curves lose convergence, and while the overall trend is maintained, there is less tendency to damp. Convergence is lost for $\tau > 10^{-3}$ and it is lost more severely than in the linear regime

linear modes are responsible. We are plotting the energy growth rates, so each curve has a constant (linear) and a variable (nonlinear) piece. Since the shape of the curves is nearly independent of τ, the linear numerics (Eqs. (8c)–(8i)) are the limiting factor. Again one can see that too large a timestep results in too much adiabaticity and thus less tendency to damp. The second-order accuracy of the nonlinear operations prevents any problems with them, as is also suggested by the higher degree of energy conservation. Due to the linear terms, the optimum value for timestep is still 10^{-3}.

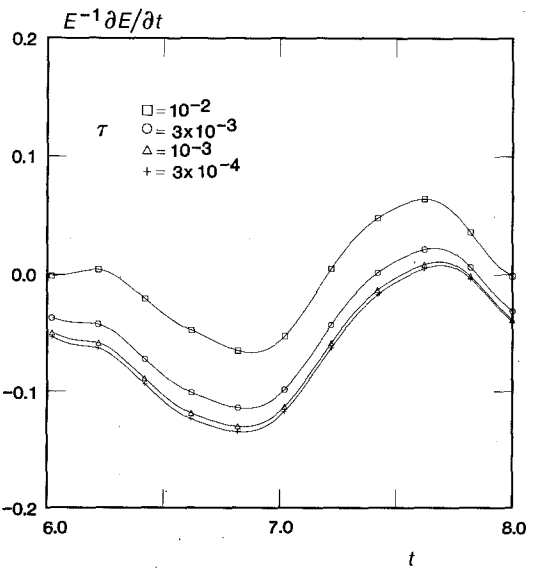

FIG. 7. The same runs as in Fig. 6, comparing the nonlinear energy growth rates. Convergence is attained for $\tau \leqslant 10^{-3}$.

The next test involved the same set-up for the timestep test except that the parameter varied was $\mu_\perp$, which took the four values 10^{-2}, 10^{-3}, 10^{-4}, and 10^{-5}. The total energy spectra for each of these runs are compared in Fig. 8, which uses the same labelling scheme as in Fig. 6. As expected, most of the difference is at the highest mode numbers. Excepting the $\mu_\perp = 10^{-2}$ case, divergence is confined below the 10^{-3} level of the spectrum. For $\mu_\perp \leqslant 10^{-4}$ the high l's are not sufficiently damped, and the runs will eventually become unstable due to pile-up of energy in that part of k_y-space. The reason that $\mu_\perp$ is not set higher than 10^{-3} is also seen in Fig. 9, in which the total energy decay rates for the different $\mu_\perp$ values are compared. After the initial adjustment period, the decay rate becomes independent of $\mu_\perp$ for $\mu_\perp \leqslant 10^{-3}$. However, the value 10^{-2} changes the energy growth curve considerably. Also, as seen in Fig. 8, this large a $\mu_\perp$ has too much effect on the spectrum for modes $l \gtrsim 10$, a region still containing appreciable energy. However, the smallest values have insufficient dissipation at high l. Thus, the artificial diffusion coefficient is usually set at $\mu_\perp = 10^{-3}$. Moreover, this may be taken as indication that 256 points in the x-direction are marginally sufficient for the existence of an appreciable window between too much and too little viscosity. Simulations with less resolution will not have such a window at all.

The final test concerns the effect of the boundary placement on the results. The same run as before was used to compare x_L values of 10.0, 20.0, and 40.0. Recall from this test on the linear scheme that the outgoing waves were adequately accommodated for $x_L \geqslant 20.0$ but that 10.0 was insufficient. The total energy spectra for each of these runs are compared in Fig. 10, which uses the same labelling scheme as

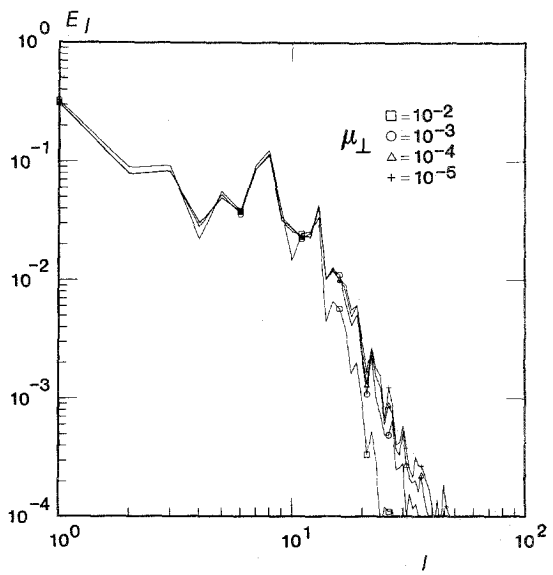

FIG. 8. Effect on the total energy (E) spectrum of varying the artificial diffusion. Individual spectra are labelled with the marker shown according to the value of $\mu_\perp$ used. l is the mode number.

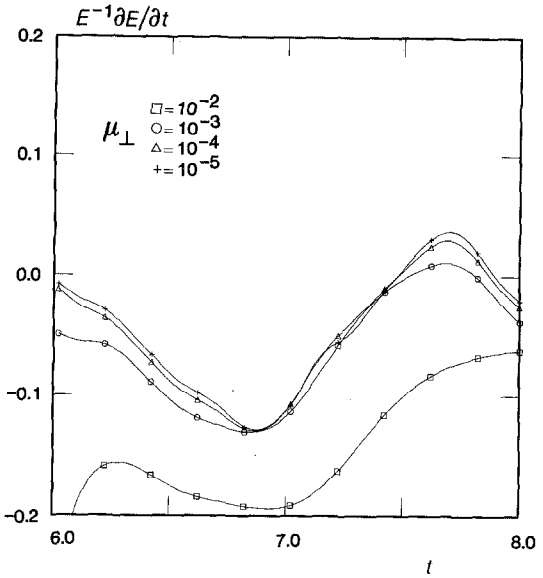

FIG. 9. The same runs as in Fig. 8, comparing the nonlinear energy growth rates. Convergence is adequate for $\mu_\perp \leqslant 10^{-3}$.

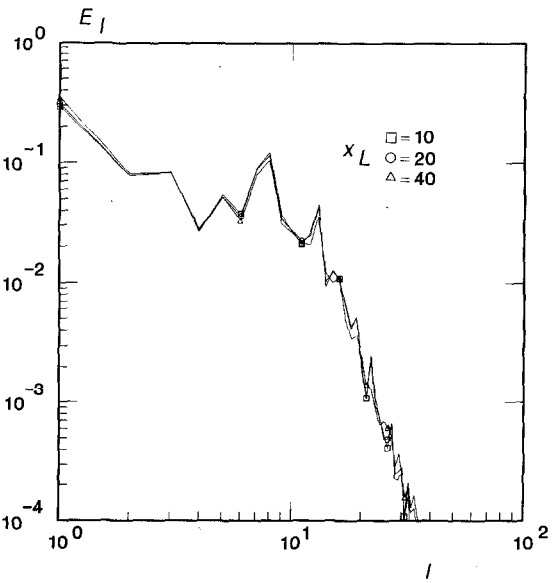

FIG. 10. Effect on the total energy (E) spectrum of varying the boundary. Individual spectra are labelled with the marker shown according to the value of x_L used. l is the mode number.

in Fig. 6. Sharp convergence is seen between the lower two values. Small-scale differences in the $x_L = 40.0$ case are attributable to the loss of resolution in the x-direction caused by the scale expansion. When x_L is doubled, the x-resolution is halved. In this case there is not sufficient breadth in the k_x-spectrum for the cascade process and energy is piling up. This shows up in the k_y-spectrum as a result of the tendency of small-scale turbulence to isotropise. The decay curves, shown in Fig. 11, lend support to this interpretation. The loss of resolution leads to a loss of convergence, shown by the $x_L = 40.0$ curve. However, the other two converge very well. Thus, even though there is not enough room for the sound waves to dissipate for $x_L = 10.0$ they are having little effect on the energetics at this point. Recalling the test on the linear scheme, however, leaves $x_L = 20.0$ as the only acceptable value. It alone satisfies both tests. This is another indication of marginal x-space resolution, another window which disappears for simulations with less resolution than that used here.

An important point is made by the success of these tests. That is the question of time resolution of the various processes represented by the terms in the equations. Paramount is the presence of both hydrodynamic and adiabatic regions within the computational domain. This would suggest that the resistive diffusion responsible for adiabatisation of the electron fluid need be time-resolved everywhere, or there should be too much dissipation resulting from the numerical scheme, the usual trade-off with implicit methods. That is not the case for the scheme of Eqs. (8a)–(8i)), for the reason that the implicit pieces are not blindly inverted together.

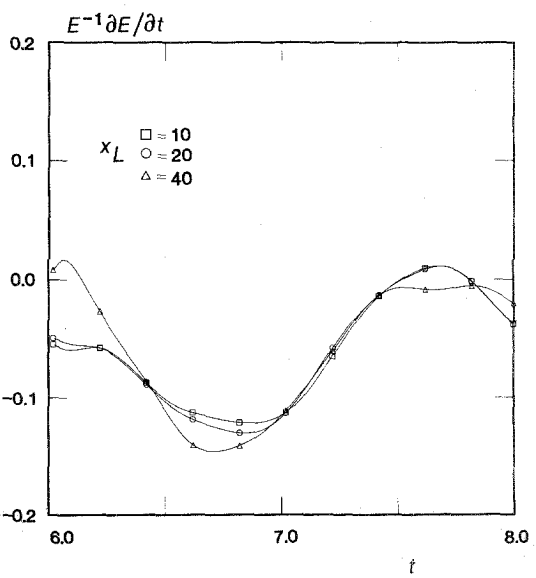

FIG. 11. The same runs as in Fig. 10, comparing the nonlinear energy growth rates. Non-convergence for $x_L = 40.0$ is due to loss of resolution.

A stepping order is chosen which allows n and ϕ to relax towards each other in the adiabatic region without trying to track each other reactively. The result is a scheme with very little inherent dissipation, as can be inferred from the tests on the linear growth rate and $\mu_\perp$. In fact, when errors are made with the timestep the tendency is toward growth, as too large a τ causes spurious adiabaticity rather than dissipation. Thus, the resistive dissipation process responsible for the adiabaticity need only be time-resolved where the fluctuation energy lives in xk_y-space and where the fluctuations are not adiabatic. The other regions are taken care of automatically. Because of the amount of effort currently being put into drift-wave simulations with much less resolution than the present treatment [8–10, 20] the importance of high resolution cannot be overstated. The present work contains adequate but marginal resolution, as is clearly shown by the tests. Anything less will either fail the convergence test or have so much artificial dissipation as to heavily influence the results.

VII. Discussion

A split-timestep, implicit scheme for managing the problems which may come in high-resolution simulations of fluid plasma turbulence has been presented. The linear coupling terms which become large for the highest modes are stabilised by the numerical scheme which evaluates them in an implicit manner that does not depend on simultaneous inversion of the coupled equations. This carries the advantages of implicit algorithms without resorting to the inversion of very large block tridiagonal matrices, which would be needed because of the coupling between equations. Great advantage is taken of the fact that time resolution of the process represented by the coupling terms is necessary only where in xk_y-space the fluctuations are appreciable. The splitting and operation order allow the use of a second-order accurate treatment where it is most needed: in the nonlinear convolutions, which must be evaluated explicitly. The placement of the inversion of D allows it to have its desired effect on the spectrum without interfering with the cancellation between the coupling terms where these are large. The present scheme very accurately represents the basic characteristics of drift-wave turbulence such as spectra, coherence properties, and spatial correlations as well as its time-dependent properties. It should be useful in making other problems tractable as well.

Acknowledgments

The author would like to thank Dr. J.-N. LeBoeuf for extensive discussions of numerical problems in shear-flow simulations that had much bearing on the algorithm presented here, Dr. P. H. Diamond for consulations on the importance of coherent structures and turbulent statistics, J. E. Sedlak for the use of his shooting code in obtaining independent linear growth rates against which to check the scheme, and Drs. LeBoeuf and P. W. Terry for helpful criticism of the manuscript. This work was supported by the U.S. Department of Energy, Contract DEFG0580ET53088.

REFERENCES

1. P. C. LIEWER, *Nucl. Fusion* **25**, 543 (1985).
2. P. W. TERRY AND P. H. DIAMOND, *Phys. Fluids* **28**, 1419 (1985).
3. L. D. PEARLSTEIN AND H. L. BERK, *Phys. Rev. Lett.* **23**, 220 (1969).
4. L. CHEN AND C. Z. CHENG, *Phys. Fluids* **23**, 2249 (1980).
5. C. S. LIU, M. N. ROSENBLUTH, AND W. M. TANG, *Phys. Fluids* **19**, 1040 (1976).
6. A. HASEGAWA AND K. MIMA, *Phys. Rev. Lett.* **39**, 205 (1977).
7. P. W. TERRY AND C. W. HORTON, *Phys. Fluids* **26**, 106 (1983).
8. D. BISKAMP, *Phys. Lett. A* **109**, 34 (1985).
9. M. WAKATANI AND A. HASEGAWA, *Phys. Fluids* **27**, 611 (1984).
10. R. E. WALTZ, *Phys. Fluids* **28**, 577 (1985).
11. S. I. BRAGINSKII, in *Reviews of Plasma Physics*, edited by M. A. Leontovich (Consultants Bureau, New York, 1965), Vol. 1, p. 205.
12. B. D. SCOTT, Ph. D. dissertation, Physics Publ. 85–186, University of Maryland, 1985 (unpublished).
13. R. D. RICHTMEYER AND K. W. MORTON, *Difference Methods for Initial-value Problems*, 2nd ed. (Interscience, New York, 1967).
14. D. GOTTLIEB AND S. A. ORSZAG, *Numerical Analysis of Spectral Methods: Theory and Applications*, CBMS-NSF Regional Conference Series in Applied Mathematics Vol. 26 (SIAM, Philadelphia 1977).
15. J. R. HERRING AND J. C. MCWILLIAMS, *J. Fluid Mech.* **153**, 259 (1984).
16. J. C. MCWILLIAMS, *J. Fluid Mech.* **146**, 21 (1984).
17. D. S. HARNED AND D. D. SCHNACK, *J. Comput. Phys.* **65**, 57 (1986); D. S. HARNED AND W. KERNER, *J. Comput. Phys.* **60**, 62 (1985).
18. A good discussion of moments as applied to drift-wave turbulence can be found in P. W. Terry, Ph. D. dissertation, University of Texas, 1981 (unpublished).
19. J. E. SEDLAK, private communication.
20. R. E. WALTZ, *Phys. Fluids* **26**, 169 (1983); R. E. WALTZ, *Phys. Fluids* **29**, 3684 (1986).